

Studies of WW and WZ production and limits on anomalous WW γ and WWZ couplings

B. Abbott,⁴⁵ M. Abolins,⁴² V. Abramov,¹⁸ B. S. Acharya,¹¹ I. Adam,⁴⁴ D. L. Adams,⁵⁴ M. Adams,²⁸ S. Ahn,²⁷ V. Akimov,¹⁶ G. A. Alves,² N. Amos,⁴¹ E. W. Anderson,³⁴ M. M. Baarmand,⁴⁷ V. V. Babintsev,¹⁸ L. Babukhadia,²⁰ A. Baden,³⁸ B. Baldin,²⁷ S. Banerjee,¹¹ J. Bantly,⁵¹ E. Barberis,²¹ P. Baringer,³⁵ J. F. Bartlett,²⁷ A. Belyaev,¹⁷ S. B. Beri,⁹ I. Bertram,¹⁹ V. A. Bezzubov,¹⁸ P. C. Bhat,²⁷ V. Bhatnagar,⁹ M. Bhattacharjee,⁴⁷ N. Biswas,³² G. Blazey,²⁹ S. Blessing,²⁵ P. Bloom,²² A. Boehnlein,²⁷ N. I. Bojko,¹⁸ F. Borchering,²⁷ C. Boswell,²⁴ A. Brandt,²⁷ R. Breedon,²² G. Briskin,⁵¹ R. Brock,⁴² A. Bross,²⁷ D. Buchholz,³⁰ V. S. Burtovoi,¹⁸ J. M. Butler,³⁹ W. Carvalho,² D. Casey,⁴² Z. Casilum,⁴⁷ H. Castilla-Valdez,¹⁴ D. Chakraborty,⁴⁷ S. V. Chekulaev,¹⁸ W. Chen,⁴⁷ S. Choi,¹³ S. Chopra,²⁵ B. C. Choudhary,²⁴ J. H. Christenson,²⁷ M. Chung,²⁸ D. Claes,⁴³ A. R. Clark,²¹ W. G. Cobau,³⁸ J. Cochran,²⁴ L. Coney,³² W. E. Cooper,²⁷ D. Coppers,³⁵ C. Cretsinger,⁴⁶ D. Cullen-Vidal,⁵¹ M. A. C. Cummings,²⁹ D. Cutts,⁵¹ O. I. Dahl,²¹ K. Davis,²⁰ K. De,⁵² K. Del Signore,⁴¹ M. Demarteau,²⁷ D. Denisov,²⁷ S. P. Denisov,¹⁸ H. T. Diehl,²⁷ M. Diesburg,²⁷ G. Di Loreto,⁴² P. Draper,⁵² Y. Ducros,⁸ L. V. Dudko,¹⁷ S. R. Dugad,¹¹ A. Dyshkant,¹⁸ D. Edmunds,⁴² J. Ellison,²⁴ V. D. Elvira,⁴⁷ R. Engelmann,⁴⁷ S. Eno,³⁸ G. Eppley,⁵⁴ P. Ermolov,¹⁷ O. V. Eroshin,¹⁸ H. Evans,⁴⁴ V. N. Evdokimov,¹⁸ T. Fahland,²³ M. K. Fatyga,⁴⁶ S. Feher,²⁷ D. Fein,²⁰ T. Ferbel,⁴⁶ H. E. Fisk,²⁷ Y. Fisyak,⁴⁸ E. Flattum,²⁷ G. E. Forden,²⁰ M. Fortner,²⁹ K. C. Frame,⁴² S. Fuess,²⁷ E. Gallas,²⁷ A. N. Galyaev,¹⁸ P. Gartung,²⁴ V. Gavrilov,¹⁶ T. L. Geld,⁴² R. J. Genik II,⁴² K. Genser,²⁷ C. E. Gerber,²⁷ Y. Gershtein,⁵¹ B. Gibbard,⁴⁸ B. Gobbi,³⁰ B. Gómez,⁵ G. Gómez,³⁸ P. I. Goncharov,¹⁸ J. L. González Solís,¹⁴ H. Gordon,⁴⁸ L. T. Goss,⁵³ K. Gounder,²⁴ A. Goussiou,⁴⁷ N. Graf,⁴⁸ P. D. Grannis,⁴⁷ D. R. Green,²⁷ J. A. Green,³⁴ H. Greenlee,²⁷ S. Grinstein,¹ P. Grudberg,²¹ S. Grünendahl,²⁷ G. Guglielmo,⁵⁰ J. A. Guida,²⁰ J. M. Guida,⁵¹ A. Gupta,¹¹ S. N. Gurzhiev,¹⁸ G. Gutierrez,²⁷ P. Gutierrez,⁵⁰ N. J. Hadley,³⁸ H. Haggerty,²⁷ S. Hagopian,²⁵ V. Hagopian,²⁵ K. S. Hahn,⁴⁶ R. E. Hall,²³ P. Hanlet,⁴⁰ S. Hansen,²⁷ J. M. Hauptman,³⁴ C. Hays,⁴⁴ C. Hebert,³⁵ D. Hedin,²⁹ A. P. Heinson,²⁴ U. Heintz,³⁹ R. Hernández-Montoya,¹⁴ T. Heuring,²⁵ R. Hirosky,²⁸ J. D. Hobbs,⁴⁷ B. Hoeneisen,⁶ J. S. Hoftun,⁵¹ F. Hsieh,⁴¹ Tong Hu,³¹ A. S. Ito,²⁷ S. A. Jerger,⁴² R. Jesik,³¹ T. Joffe-Minor,³⁰ K. Johns,²⁰ M. Johnson,²⁷ A. Jonckheere,²⁷ M. Jones,²⁶ H. Jöstlein,²⁷ S. Y. Jun,³⁰ C. K. Jung,⁴⁷ S. Kahn,⁴⁸ D. Karmanov,¹⁷ D. Karmgard,²⁵ R. Kehoe,³² S. K. Kim,¹³ B. Klima,²⁷ C. Klopfenstein,²² W. Ko,²² J. M. Kohli,⁹ D. Koltick,³³ A. V. Kostitskiy,¹⁸ J. Kotcher,⁴⁸ A. V. Kotwal,⁴⁴ A. V. Kozelov,¹⁸ E. A. Kozlovsky,¹⁸ J. Krane,³⁴ M. R. Krishnaswamy,¹¹ S. Krzywdzinski,²⁷ M. Kubantsev,³⁶ S. Kuleshov,¹⁶ Y. Kulik,⁴⁷ S. Kunori,³⁸ F. Landry,⁴² G. Landsberg,⁵¹ A. Leflat,¹⁷ J. Li,⁵² Q. Z. Li,²⁷ J. G. R. Lima,³ D. Lincoln,²⁷ S. L. Linn,²⁵ J. Linnemann,⁴² R. Lipton,²⁷ A. Lucotte,⁴⁷ L. Lueking,²⁷ A. L. Lyon,³⁸ A. K. A. Maciel,²⁹ R. J. Madaras,²¹ R. Madden,²⁵ L. Magaña-Mendoza,¹⁴ V. Manankov,¹⁷ S. Mani,²² H. S. Mao,⁴ R. Markeloff,²⁹ T. Marshall,³¹ M. I. Martin,²⁷ R. D. Martin,²⁸ K. M. Mauritz,³⁴ B. May,³⁰ A. A. Mayorov,¹⁸ R. McCarthy,⁴⁷ J. McDonald,²⁵ T. McKibben,²⁸ J. McKinley,⁴² T. McMahan,⁴⁹ H. L. Melanson,²⁷ M. Merkin,¹⁷ K. W. Merritt,²⁷ C. Miao,⁵¹ H. Miettinen,⁵⁴ A. Mincer,⁴⁵ C. S. Mishra,²⁷ N. Mokhov,²⁷ N. K. Mondal,¹¹ H. E. Montgomery,²⁷ P. Mooney,⁵ M. Mostafa,¹ H. da Motta,² C. Murphy,²⁸ F. Nang,²⁰ M. Narain,³⁹ V. S. Narasimham,¹¹ A. Narayanan,²⁰ H. A. Neal,⁴¹ J. P. Negret,⁵ P. Nemethy,⁴⁵ D. Norman,⁵³ L. Oesch,⁴¹ V. Oguri,³ N. Oshima,²⁷ D. Owen,⁴² P. Padley,⁵⁴ A. Para,²⁷ N. Parashar,⁴⁰ Y. M. Park,¹² R. Partridge,⁵¹ N. Parua,⁷ M. Paterno,⁴⁶ B. Pawlik,¹⁵ J. Perkins,⁵² M. Peters,²⁶ R. Piegai,¹ H. Piekarczyk,²⁵ Y. Pischalnikov,³³ B. G. Pope,⁴² H. B. Prosper,²⁵ S. Protopopescu,⁴⁸ J. Qian,⁴¹ P. Z. Quintas,²⁷ R. Raja,²⁷ S. Rajagopalan,⁴⁸ O. Ramirez,²⁸ N. W. Reay,³⁶ S. Reucroft,⁴⁰ M. Rijssenbeek,⁴⁷ T. Rockwell,⁴² M. Roco,²⁷ P. Rubinov,³⁰ R. Ruchti,³² J. Rutherford,²⁰ A. Sánchez-Hernández,¹⁴ A. Santoro,² L. Sawyer,³⁷ R. D. Schamberger,⁴⁷ H. Schellman,³⁰ J. Sculli,⁴⁵ E. Shabalina,¹⁷ C. Shaffer,²⁵ H. C. Shankar,¹¹ R. K. Shivpuri,¹⁰ D. Shpakov,⁴⁷ M. Shupe,²⁰ R. A. Sidwell,³⁶ H. Singh,²⁴ J. B. Singh,⁹ V. Sirotenko,²⁹ E. Smith,⁵⁰ R. P. Smith,²⁷ R. Snihur,³⁰ G. R. Snow,⁴³ J. Snow,⁴⁹ S. Snyder,⁴⁸ J. Solomon,²⁸ M. Sosebee,⁵² N. Sotnikova,¹⁷ M. Souza,² N. R. Stanton,³⁶ G. Steinbrück,⁵⁰ R. W. Stephens,⁵² M. L. Stevenson,²¹ F. Stichelbaut,⁴⁸ D. Stoker,²³ V. Stolin,¹⁶ D. A. Stoyanova,¹⁸ M. Strauss,⁵⁰ K. Streets,⁴⁵ M. Strovink,²¹ A. Sznajder,² P. Tamburello,³⁸ J. Tarazi,²³ M. Tartaglia,²⁷ T. L. T. Thomas,³⁰ J. Thompson,³⁸ D. Toback,³⁸ T. G. Trippe,²¹ P. M. Tuts,⁴⁴ V. Vaniev,¹⁸ N. Varelas,²⁸ E. W. Varnes,²¹ A. A. Volkov,¹⁸ A. P. Vorobiev,¹⁸ H. D. Wahl,²⁵ G. Wang,²⁵ J. Warchol,³² G. Watts,⁵¹ M. Wayne,³² H. Weerts,⁴² A. White,⁵² J. T. White,⁵³ J. A. Wightman,³⁴ S. Willis,²⁹ S. J. Wimpenny,²⁴ J. V. D. Wirjawan,⁵³ J. Womersley,²⁷ D. R. Wood,⁴⁰ R. Yamada,²⁷ P. Yamin,⁴⁸ T. Yasuda,⁴⁰ P. Yepes,⁵⁴ K. Yip,²⁷ C. Yoshikawa,²⁶ S. Youssef,²⁵ J. Yu,²⁷ Y. Yu,¹³ B. Zhang,⁴ Z. Zhou,³⁴ Z. H. Zhu,⁴⁶ M. Zielinski,⁴⁶ D. Zieminska,³¹ A. Zieminski,³¹ V. Zutshi,⁴⁶ E. G. Zverev,¹⁷ and A. Zylberstein⁸

(DØ Collaboration)

¹Universidad de Buenos Aires, Buenos Aires, Argentina²LAFEX, Centro Brasileiro de Pesquisas Físicas, Rio de Janeiro, Brazil³Universidade do Estado do Rio de Janeiro, Rio de Janeiro, Brazil⁴Institute of High Energy Physics, Beijing, People's Republic of China⁵Universidad de los Andes, Bogotá, Colombia⁶Universidad San Francisco de Quito, Quito, Ecuador⁷Institut des Sciences Nucléaires, IN2P3-CNRS, Université de Grenoble I, Grenoble, France

- ⁸DAPNIA/Service de Physique des Particules, CEA, Saclay, France
⁹Panjab University, Chandigarh, India
¹⁰Delhi University, Delhi, India
¹¹Tata Institute of Fundamental Research, Mumbai, India
¹²Kyungshung University, Pusan, Korea
¹³Seoul National University, Seoul, Korea
¹⁴CINVESTAV, Mexico City, Mexico
¹⁵Institute of Nuclear Physics, Kraków, Poland
¹⁶Institute for Theoretical and Experimental Physics, Moscow, Russia
¹⁷Moscow State University, Moscow, Russia
¹⁸Institute for High Energy Physics, Protvino, Russia
¹⁹Lancaster University, Lancaster, United Kingdom
²⁰University of Arizona, Tucson, Arizona 85721
²¹Lawrence Berkeley National Laboratory and University of California, Berkeley, California 94720
²²University of California, Davis, California 95616
²³University of California, Irvine, California 92697
²⁴University of California, Riverside, California 92521
²⁵Florida State University, Tallahassee, Florida 32306
²⁶University of Hawaii, Honolulu, Hawaii 96822
²⁷Fermi National Accelerator Laboratory, Batavia, Illinois 60510
²⁸University of Illinois at Chicago, Chicago, Illinois 60607
²⁹Northern Illinois University, DeKalb, Illinois 60115
³⁰Northwestern University, Evanston, Illinois 60208
³¹Indiana University, Bloomington, Indiana 47405
³²University of Notre Dame, Notre Dame, Indiana 46556
³³Purdue University, West Lafayette, Indiana 47907
³⁴Iowa State University, Ames, Iowa 50011
³⁵University of Kansas, Lawrence, Kansas 66045
³⁶Kansas State University, Manhattan, Kansas 66506
³⁷Louisiana Tech University, Ruston, Louisiana 71272
³⁸University of Maryland, College Park, Maryland 20742
³⁹Boston University, Boston, Massachusetts 02215
⁴⁰Northeastern University, Boston, Massachusetts 02115
⁴¹University of Michigan, Ann Arbor, Michigan 48109
⁴²Michigan State University, East Lansing, Michigan 48824
⁴³University of Nebraska, Lincoln, Nebraska 68588
⁴⁴Columbia University, New York, New York 10027
⁴⁵New York University, New York, New York 10003
⁴⁶University of Rochester, Rochester, New York 14627
⁴⁷State University of New York, Stony Brook, New York 11794
⁴⁸Brookhaven National Laboratory, Upton, New York 11973
⁴⁹Langston University, Langston, Oklahoma 73050
⁵⁰University of Oklahoma, Norman, Oklahoma 73019
⁵¹Brown University, Providence, Rhode Island 02912
⁵²University of Texas, Arlington, Texas 76019
⁵³Texas A&M University, College Station, Texas 77843
⁵⁴Rice University, Houston, Texas 77005
- (Received 4 May 1999; published 8 September 1999)

Evidence of anomalous WW and WZ production was sought in $p\bar{p}$ collisions at a center-of-mass energy of $\sqrt{s} = 1.8$ TeV. The final states $WW(WZ) \rightarrow \mu\nu$ jet jet + X , $WZ \rightarrow \mu\nu ee + X$ and $WZ \rightarrow e\nu ee + X$ were studied using a data sample corresponding to an integrated luminosity of approximately 90 pb^{-1} . No evidence of anomalous diboson production was found. Limits were set on anomalous $WW\gamma$ and WWZ couplings and were combined with our previous results. The combined 95% confidence level anomalous coupling limits for $\Lambda = 2$ TeV are $-0.25 \leq \Delta\kappa \leq 0.39$ ($\lambda = 0$) and $-0.18 \leq \lambda \leq 0.19$ ($\Delta\kappa = 0$), assuming the $WW\gamma$ couplings are equal to the WWZ couplings. [S0556-2821(99)02619-3]

PACS number(s): 14.70.Fm, 13.40.Em, 13.85.Rm, 14.70.Hp

I. INTRODUCTION

The gauge theory of the electroweak interactions contains a striking feature. Unlike the electrically neutral photon in quantum electrodynamics (QED), the weak vector bosons carry weak charge. Consequently, whereas in QED there are no photon-photon couplings, the weak vector bosons interact among themselves through the trilinear and quartic gauge boson vertices.

A formalism has been developed to describe the $WW\gamma$ and WWZ vertices for the most general gauge boson self-interactions [1,2]. The Lorentz invariant effective Lagrangian for the gauge boson self-interactions contains 14 dimensionless couplings, seven each for $WW\gamma$ and WWZ :

$$\begin{aligned} \mathcal{L}_{WWV}/g_{WWV} = & ig_1^V (W_{\mu\nu}^\dagger W^\mu V^\nu - W_\mu^\dagger V_\nu W^{\mu\nu}) \\ & + i\kappa_V W_\mu^\dagger W_\nu V^{\mu\nu} + i \frac{\lambda_V}{M_W^2} W_{\lambda\mu}^\dagger W_\nu^\mu V^{\nu\lambda} \\ & - g_4^V W_\mu^\dagger W_\nu (\partial^\mu V^\nu + \partial^\nu V^\mu) \\ & + g_5^V \epsilon^{\mu\nu\rho\alpha} (W_\mu^\dagger \vec{\partial}_\rho W_\nu) V_\alpha + i\tilde{\kappa}_V W_\mu^\dagger W_\nu \tilde{V}^{\mu\nu} \\ & + \frac{i\tilde{\lambda}_V}{M_W^2} W_{\lambda\mu}^\dagger W_\nu^\mu \tilde{V}^{\nu\lambda}, \end{aligned}$$

where W^μ denotes the W^- field, $W_{\mu\nu} = \partial_\mu W_\nu - \partial_\nu W_\mu$, $V_{\mu\nu} = \partial_\mu V_\nu - \partial_\nu V_\mu$, $\tilde{V}_{\mu\nu} = \frac{1}{2} \epsilon_{\mu\nu\rho\alpha} V^{\rho\alpha}$, and $(A \vec{\partial}_\mu B) = A(\partial_\mu B) - (\partial_\mu A)B$, $V = \gamma$ and Z , and M_W is the mass of the W boson. The overall coupling parameters g_{WWV} are $g_{WW\gamma} = -e$ and $g_{WWZ} = -e \cot \theta_w$, as in the standard model (SM), where e and θ_w are the positron charge and the weak mixing angle. The couplings λ_V and κ_V conserve C and P . The couplings g_4^V are odd under CP and C , g_5^V are odd under C and P , and $\tilde{\kappa}_V$ and $\tilde{\lambda}_V$ are odd under CP and P . In the SM, all the couplings are zero at the tree level with the exception of g_1^V and κ_V ($g_1^\gamma = g_1^Z = \kappa_\gamma = \kappa_Z = 1$), and $\Delta\kappa_V$ and Δg_1^Z are defined as $\kappa_V - 1$ and $g_1^Z - 1$, respectively. Electromagnetic gauge invariance restricts g_1^γ , g_4^γ , and g_5^γ to the SM values of 1, 0, and 0. The CP -violating $WW\gamma$ couplings $\tilde{\lambda}_\gamma$ and $\tilde{\kappa}_\gamma$ have been tightly constrained by measurements of the neutron electric dipole moment to $|\tilde{\kappa}_\gamma|, |\tilde{\lambda}_\gamma| < 10^{-3}$ [3].

With non-SM coupling parameters, the amplitudes for gauge boson pair production grow with energy, eventually violating tree-level unitarity. The unitarity violation is avoided by parametrizing the anomalous couplings as dipole form factors with a cutoff scale, Λ . Then the anomalous couplings take a form, for example,

$$\Delta\kappa(\hat{s}) = \frac{\Delta\kappa}{(1 + \hat{s}/\Lambda^2)^2},$$

where \hat{s} is the invariant mass of the vector boson pair and $\Delta\kappa$ is the coupling value at the low energy limit [4]. Λ is physically interpreted as the mass scale where the new phenomenon which is responsible for the anomalous couplings would be directly observable.

Direct tests of the trilinear couplings are provided by e^+e^- and $p\bar{p}$ colliders through production of gauge boson pairs, in particular by $e^+e^- \rightarrow W^+W^-$, $Z\gamma$, and ZZ and by $p\bar{p} \rightarrow W^\pm\gamma$, W^+W^- , $W^\pm Z$, $Z\gamma$, and ZZ . The experiments seek to measure, or otherwise place limits on, trilinear couplings and to retain sensitivity to the appearance of new physical phenomena. The signature for anomalous trilinear couplings is an excess of gauge boson pairs, particularly for large values of the invariant mass of the gauge boson pair and for large values of gauge boson transverse momentum p_T .

Limits on these couplings are often obtained under the assumption that the $WW\gamma$ and WWZ couplings are equal ($g_1^\gamma = g_1^Z$, $\Delta\kappa_\gamma = \Delta\kappa_Z$, and $\lambda_\gamma = \lambda_Z$). Another set of parameters, $\alpha_{B\phi}$, $\alpha_{W\phi}$, and α_W , is similarly motivated by $SU(2)_L \times U(1)_Y$ gauge invariance. These couplings are linear combinations of λ_V , $\Delta\kappa_V$, and Δg_1^Z such that $\alpha_{B\phi} = \Delta\kappa_\gamma - \Delta g_1^Z \cos^2 \theta_w$, $\alpha_{W\phi} = \Delta g_1^Z \cos^2 \theta_w$, and $\alpha_W = \lambda_\gamma$ with the constraints that $\Delta\kappa_Z = -\Delta\kappa_\gamma \tan^2 \theta_w + \Delta g_1^Z$ and $\lambda_\gamma = \lambda_Z$. Adding the additional constraint that $\alpha_{B\phi} = \alpha_{W\phi}$ yields [5] the Hagiwara-Ishihara-Szalapski-Zeppenfeld (HISZ) relations used by the DØ and Collider Detector at Fermilab (CDF) Collaborations.

The DØ Collaboration has previously performed several searches for anomalous $WW\gamma$ and WWZ couplings. Studies [6,7] of $p\bar{p} \rightarrow W\gamma + X$ have shown that the transverse energy spectrum of the photons agreed with that expected from SM production. Searches [8,9] for an excess of $p\bar{p} \rightarrow WW + X$, where the W bosons each decayed to $l\nu$ ($l = e$ or μ), yielded events which matched the SM prediction. Further, the p_T spectrum of the charged leptons agreed [9] with the prediction. Studies [10,11] of the processes $p\bar{p} \rightarrow WW + X$ and $p\bar{p} \rightarrow WZ + X$, where one W boson decayed to an electron or positron and the corresponding antineutrino or neutrino and the other vector boson decayed to a quark-antiquark pair manifested as jets, yielded no excess of events and a W boson transverse energy spectrum which matched the expected background plus SM signal. Limits on anomalous $WW\gamma$ and WWZ couplings were derived from each of these analyses. Several [6,8,10] of these analyses were presented in detail in Ref. [12]. The results of all of these analyses were combined [13], using the method described in Ref. [12], to form our most restrictive limits on anomalous $WW\gamma$ and WWZ couplings.

Limits on the $WW\gamma$ couplings have been set by the UA2 and CDF Collaborations from the properties of $W + \gamma$ events [14,15] and by the L3 Collaboration [16] from the rate of single W boson production at $\sqrt{s} = 172$ GeV. Both the WWZ and $WW\gamma$ couplings have been studied by several experiments. CDF has searched for anomalous WW and WZ production [17,18] and the four experiments at the CERN e^+e^- collider LEP have studied the properties of WW events [19–26].

In this paper two new analyses resulting from a study of $p\bar{p}$ collisions at a center-of-mass energy of $\sqrt{s} = 1.8$ TeV are presented. The collisions were recorded at DØ during the 1994–1995 and 1996 collider runs of the Fermilab Tevatron.

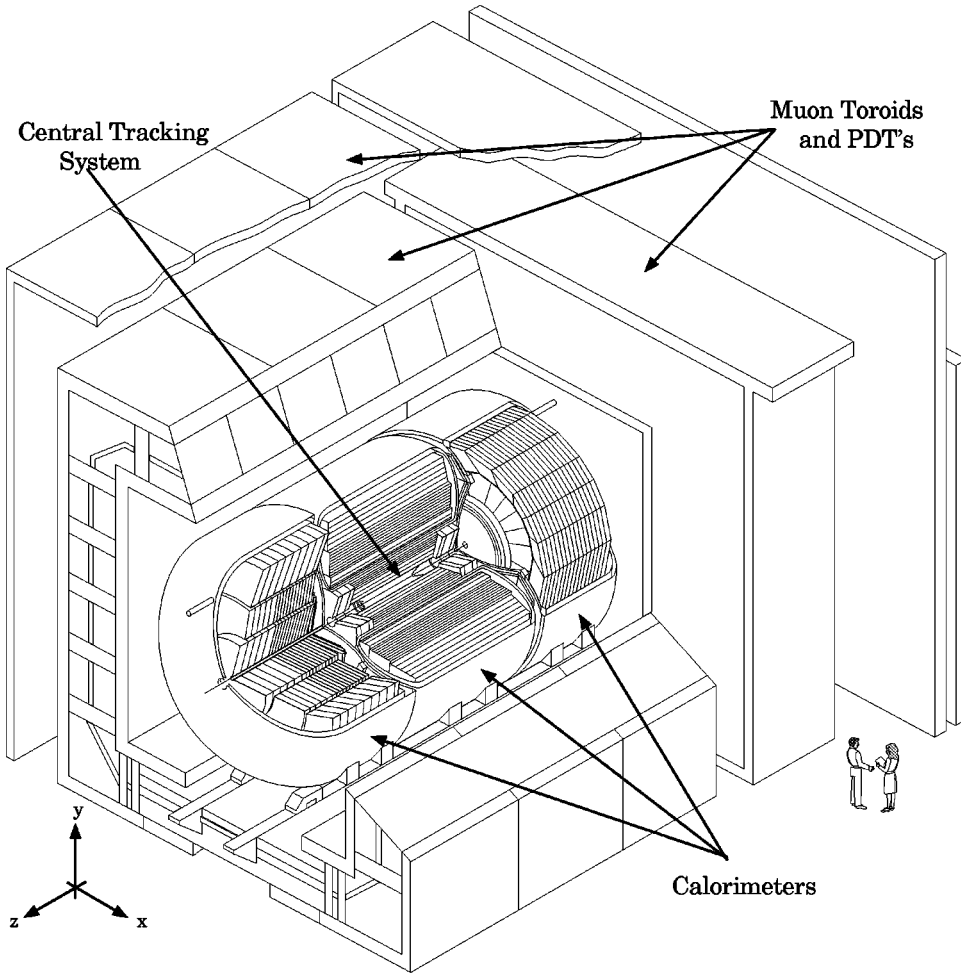


FIG. 1. Isometric view of the DØ detector. Also shown are the calorimeter support platform, the Tevatron beampipe centered within the calorimeter, and the Main Ring beampipe which penetrated the muon system and calorimeter above the detector center.

The first analysis is a search for WZ production which provides a test of anomalous couplings unique among the gauge boson pair analyses. WZ production is sensitive only to the WW couplings, not the $WW\gamma$ couplings. In this analysis the collisions were searched for WZ events where the Z boson decayed to ee and the W boson decayed to either $e\nu$ or $\mu\nu$. The expected SM WZ signal and the background were approximately equal in size and both were expected to be small. The number of events observed was compared with that expected from anomalous WZ production in the presence of background to set upper limits on anomalous WWZ couplings.

The second analysis is a search for anomalous WW and WZ (WW/WZ) production, similar to those of Refs. [10,11], using the decay signature $W \rightarrow \mu\nu$, $W/Z \rightarrow$ hadronic jets. Because SM WW and WZ production was swamped by backgrounds from other sources of $\mu\nu jj$ events, the analysis was sensitive only to anomalous vector boson pair production. The p_T spectrum of the $\mu\nu$ system was compared to that expected from anomalous WW and WZ production plus the background, and limits on anomalous WWZ and $WW\gamma$ couplings were produced.

The paper is arranged so that the subsequent two sections present elements common to the two analyses: the detector and particle identification. The fourth section is a description of the $WZ \rightarrow ll\nu + X$ search and limits on anomalous WWZ

couplings. The next section describes the $WW/WZ \rightarrow \mu\nu jj + X$ analysis and limits on anomalous WWZ and $WW\gamma$ couplings. The sixth section contains a summary of the results of combining the anomalous coupling limits of these two analyses with those of our previous publications, producing the most restrictive anomalous $WW\gamma$ and WWZ coupling limits available to date from this experiment. Finally, the last section contains the conclusion and summary of the results presented in this paper.

II. DETECTOR

The DØ detector consisted of four main systems: a non-magnetic inner tracking system, a liquid-argon uranium calorimeter, a muon spectrometer, and a trigger system. The detector is briefly described in this section. A detailed description of the detector is available in Ref. [27]. The tracker, calorimeter, and muon system are shown in Fig. 1.

A non-magnetic central tracking system, composed of central and forward drift chambers, provided directional information for charged particles and is used in this analysis to discriminate between electrons and photons, and in muon identification.

Particle energies were measured by a liquid-argon uranium sampling calorimeter that was divided into three cryostats. The central calorimeter (CC) covered pseudorapidity

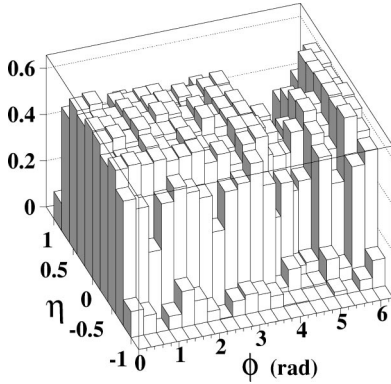


FIG. 2. The geometrical acceptance of the muon detector within the region $|\eta| \leq 1$. $\phi = 3\pi/2$ is the downward ($-\hat{y}$) direction where the calorimeter support platform breaks into the muon system three-layer geometry.

[28] $|\eta| < 1.1$, and the end calorimeters (EC) covered $1.1 < |\eta| < 4.4$. The calorimeter was transversely segmented into projective towers with $\Delta\eta \times \Delta\phi = 0.1 \times 0.1$, where ϕ is the azimuthal angle. The third layer of the electromagnetic (EM) calorimeters, where the maximum energy deposition from EM showers was expected to occur, was segmented more finely into cells with $\Delta\eta \times \Delta\phi = 0.05 \times 0.05$. The scintillator-based intercryostat detectors (ICD's), which improved the energy resolution for jets that straddled the central and end calorimeters, were inserted into the space between the cryostats. Thus, jet identification was performed in the whole calorimeter without any gap in pseudorapidity. Electron identification was performed for EM clusters with pseudorapidity $|\eta| \leq 2.5$, but the boundary between the CC and EC cryostats resulted in a gap spanning the region $1.1 \leq |\eta| \leq 1.5$.

The muon spectrometer consisted of solid-iron toroidal magnets and sets of proportional drift tubes (PDT's). It provided identification of muons and determination of their trajectories and momenta. It consisted of three layers: a layer with four planes of PDT's, located between the calorimeter and the toroid magnets, and two layers, each with three planes of PDT's, located outside the toroid magnets. Figure 2 shows the geometric acceptance of the muon detector for the region $|\eta| \leq 1$ as determined from a Monte Carlo simulation of the detector. The acceptance is nearly symmetric around $\eta = 0$. The muon momentum p was determined from its deflection angle in the magnetic field of the toroid. The momentum resolution was limited by multiple scattering in the calorimeter and toroid, knowledge of the magnetic field integral, and the accuracy of the deflection angle measurement.

A multi-level, multi-detector trigger system [12,27] was used for selecting interesting events and recording them to tape. A coincidence between hits in two hodoscopes of scintillation counters (level 0), centered around the beampipe, was required to register the presence of an inelastic collision. These counters also served as the luminosity monitor for the experiment. The level 1 and level 1.5 triggers were programmable hardware triggers which made decisions based on combinations of detector-specific algorithms. The level 2 trigger was a farm of 48 VAX 4000/60 and 4000/90 comput-

TABLE I. Measured efficiencies for electron identification in the CC and two EC's. See text for definitions of tight and loose.

Electron type	Efficiency (CC) %	Efficiency (EC) %
Loose	88.6 ± 0.3	88.4 ± 0.5
Tight	73.4 ± 0.5	67.2 ± 0.3

ers which filtered the events based on reconstruction of the information available from the front-end electronics.

III. PARTICLE IDENTIFICATION

The analyses described in this paper rely on the detector's ability to identify electrons, muons, hadronic jets, and the undetected transverse energy due to neutrinos. A brief description of the particle identification criteria is presented in this section. A more detailed description of these particle identification criteria is available in Ref. [12].

A. Electron identification

Electron candidates were identified using information from the calorimeters and tracking detectors. Electron candidates were formed from clusters, identified using a nearest-neighbor algorithm, with more than 90% of their energy in the EM layers of the calorimeter. The EM clusters had to fall within the CC ($|\eta| < 1.0$) or either EC ($1.5 < |\eta| < 2.5$). Electrons had to be isolated, had to have a shower shape consistent with that from test beam measurements, and had to have either a track that closely matched the position of the shower centroid ("tight" selection criteria) or drift chamber hits consistent with the passage of a charged particle within an azimuthal road of width $\Delta\phi = 15$ (30) milliradians for CC (EC) EM clusters ("loose" selection criteria).

The efficiency for selecting electrons with the selection criteria described above was calculated using $Z \rightarrow ee$ decays. The efficiencies for each η region and electron definition are shown in Table I. The energy resolution was $\sigma(E)/E = 14\%/\sqrt{E(\text{GeV})} \oplus 0.3\% \oplus 14\%/E(\text{GeV})$ for electrons in the CC and $\sigma(E)/E = 15.7\%/\sqrt{E(\text{GeV})} \oplus 0.3\% \oplus 29\%/E(\text{GeV})$ for electrons in the EC, where " \oplus " indicates addition in quadrature.

B. Muon identification

Muon candidates were tracks in the muon chambers which survived a number of reconstruction quality cuts. A muon was required to lie within the central region ($|\eta| < 1.0$). A muon had to pass through a region of the muon toroid with sufficient magnetic field ($\int B dl > 2.0 \text{ Tm}$). The energy deposited along the muon track in the calorimeter had to be at least that expected from a minimum-ionizing particle which on average deposits $\sim 1 \text{ GeV}$. The impact parameter of the muon with respect to the interaction point had to be less than 20 cm. The muon track was refitted with the timing, t_0 , of the muon track with respect to the collision as a floating parameter. It was required that t_0 be consistent with a muon originating from the

interaction. A slightly different t_0 cut was used in the two analyses due to the different nature of the backgrounds. Last, the muon had to be separated by $\Delta R_{\mu} \equiv \sqrt{(\Delta \eta)^2 + (\Delta \phi)^2} \geq 0.5$ from the nearest jet with $E_T \geq 8$ GeV in the event. The muon reconstruction efficiency, determined from $Z \rightarrow \mu\mu$ candidates, in the $WZ \rightarrow \mu\nu ee$ ($WW/WZ \rightarrow \mu\nu jj$) analysis for muons with $|\eta_{\mu}| < 1$ was 0.701 ± 0.031 ($0.680_{-0.080}^{+0.041}$) excluding losses due to the geometric acceptance of the muon detector. The muon momentum resolution was $\sigma(1/p) = 0.18(p-2)/p^2 \oplus 0.003$ (p in GeV/ c).

C. Jet identification and missing energy

Jets were identified [12] as clusters of calorimeter towers within a cone centered on the highest E_T tower. For the analyses described here, a cone size of $R \equiv \sqrt{(\Delta \eta)^2 + (\Delta \phi)^2} = 0.5$ was used. The energy deposited by the jet in the electromagnetic and hadronic calorimeters had to be consistent with that of an ordinary jet, thus suppressing the backgrounds from isolated noisy calorimeter cells and accelerator losses. These jet identification criteria have an efficiency of 0.96 ± 0.01 per jet. The jet energy resolution depended on the jet pseudorapidity and was approximately $\sigma(E)/E = 80\% / \sqrt{E(\text{GeV})}$.

The primary sources of missing transverse energy included neutrinos, which escaped undetected, and the energy imbalance due to the resolution of the calorimeter and muon system. Two calculations of missing transverse energy were made. The missing transverse energy which was calculated from the energy deposited in the calorimeter is referred to as $\cancel{E}_T^{\text{cal}}$. The missing energy which was calculated from the energy deposited in the calorimeter and was corrected for muons passing some loose quality cuts is referred to as \cancel{E}_T .

IV. SEARCH FOR $WZ \rightarrow \text{TRILEPTONS}$

A search for WZ production was performed in the $e\nu ee$ and $\mu\nu ee$ decay modes, taking advantage of the unusual signature consisting of three charged high- E_T leptons and the missing transverse energy due to the high- E_T neutrino.

A. Trigger and data sample

The level 1 trigger used for this study required two EM calorimeter trigger towers ($\Delta \eta \times \Delta \phi = 0.2 \times 0.2$) with $E_T > 10$ GeV. The level 2 trigger required two clusters of EM trigger towers which had $E_T > 20$ GeV and passed level 2 isolation and shower shape cuts. The efficiency of the trigger was measured as a function of the reconstructed electron E_T and found to be greater than 99% for a reconstructed $E_T > 25$ GeV. The integrated luminosity of the data sample was $92.3 \pm 5.0 \text{ pb}^{-1}$. The luminosity determination is described in Ref. [29].

B. Event selection criteria

$WZ \rightarrow e\nu ee$ events were required to have two high- E_T electrons consistent with a Z boson decay and a third electron and \cancel{E}_T consistent with a W boson decay. Specifically, at least one electron was required to satisfy the tight selection

TABLE II. Jet misidentification probabilities for tight and loose electrons. The probability is a linear function of $E_T(\text{GeV})$, $a_0 + a_1 E_T(\text{GeV})$. Uncertainties given in this table are statistical only. A systematic uncertainty of 25% was assigned to each fake probability.

Electron type	CC		EC	
	$a_0 \times 10^3$	$a_1 \times 10^5$	$a_0 \times 10^3$	$a_1 \times 10^5$
Loose	0.08 ± 0.29	2.06 ± 0.70	1.3 ± 1.0	6.31 ± 0.27
Tight	-0.17 ± 0.20	1.43 ± 0.51	0.53 ± 0.86	5.1 ± 2.3

criteria and another two were required to satisfy the tight or loose selection criteria (as defined in Sec. III A). A tight electron and one of the other electrons were required to have $E_T > 25$ GeV and the third electron to have $E_T > 10$ GeV. It was required that $\cancel{E}_T^{\text{cal}} > 15$ GeV. The invariant mass of two of the electrons had to be within the range $81 < M_{i,j} < 101 \text{ GeV}/c^2$, as expected for the decay of a Z boson. The transverse mass

$$M_T(e\nu) = \sqrt{2E_T^e \cancel{E}_T^{\text{cal}} [1 - \cos(\phi_e - \phi_\nu)]}$$

calculated using the E_T of the other electron and the $\cancel{E}_T^{\text{cal}}$ was required to be $M_T(e\nu) > 30$ GeV, as expected for the decay of a W boson. These criteria were checked for all three combinations of electrons. One event was found which passed all the selection criteria. The parameters [30] of this event are described in the Appendix.

$WZ \rightarrow \mu\nu ee$ events were required to have two high- E_T electrons as expected for a Z boson decay, and a muon and \cancel{E}_T consistent with a W boson decay. Specifically, at least one electron was required to satisfy the tight selection criteria and another was required to satisfy the tight or loose selection criteria. Both electrons had to have $E_T > 25$ GeV. Instead of the 10 GeV third electron of the $e\nu ee$ search, a muon with $p_T > 15 \text{ GeV}/c$ was required. Finally, it was required that $\cancel{E}_T > 15$ GeV. No events passed these selection criteria.

C. Background expected

The trilepton plus missing transverse energy signature demanded by the event selection has no known significant sources other than WZ production and backgrounds due to objects misidentified as leptons.

In the $e\nu ee$ channel the largest background was expected to come from Z +jet events with $Z \rightarrow ee$ and where a jet mimicked an additional electron. This background was estimated using data. Events with two electron candidates and one or more jets were selected from the same data sample used in the event selection. The kinematic event selection criteria were applied treating each jet as the third electron. The probability for a jet to mimic a tight or loose electron was determined from a sample of multijet events and was parametrized by a linear function of jet E_T for jets with E_T less than ~ 150 GeV, as given in Table II. The background was then the number of ee +jet events times the probability

of a jet mimicking the third (tight or loose) electron. This background was estimated to be $0.38 \pm 0.07(\text{stat}) \pm 0.11(\text{syst})$ events. The size of the statistical uncertainty was determined by the statistics of the $ee + \text{jets}$ sample. The systematic uncertainty was dominated by the 25% uncertainty in the probability for a jet to mimic a tight or loose electron. This latter uncertainty was due, in large part, to the uncertainty on the amount of direct photons in the multijet sample. A cross-check based on a data sample of events enriched with highly EM jets which failed the electron selection criteria gave $0.42_{-0.26}^{+0.41}$ events for this background.

In the $\mu\nu ee$ channel there were two contributions to the background, one from events with two electrons and a jet which produced an isolated muon and one from events with an electron, a muon, and a jet which mimicked an electron. Data-based methods of calculating the background were used to estimate both of these contributions to the background.

To calculate the $ee + \text{jet}$ event background, events with two electrons and a central jet were selected (this was called the “fake” sample). Each event was required to pass all selection criteria except that the jet was only required to pass the muon fiducial and kinematic selection. The number of events was then multiplied by the probability of the jet producing an isolated muon, this probability having been determined using two methods. The probability (per jet) of finding an isolated muon in a sample of multijet events with $E_T(\text{jet}) > 15 \text{ GeV}$ was found to be 1.5×10^{-5} . The number of events expected from this background was ≤ 0.002 . On the other hand, a fraction of the $ee + \text{jet}$ events contained heavy quark (b/c) jets. Assuming that all of the jets in the fake sample are heavy quark jets, a heavy-quark-enhanced fake rate was used to obtain an upper limit for this background. The probability of a jet mimicking a muon from a heavy quark (b/c) jet was found by requiring a muon (isolated or non-isolated) in the opposite hemisphere from the isolated muon in multijet events. This gave a heavy-quark-enhanced fake rate of 2.5×10^{-4} , resulting in an upper limit of $N_{\text{bkg}} = 0.022 \pm 0.004$ events. When setting limits on the cross section and coupling parameters, a smaller background estimate gives a more conservative limit. Therefore the lower estimate (≤ 0.002 events) was used in lieu of the larger (0.022 events).

The second background ($e\mu + \text{jet}$ events) was calculated using events collected with a different trigger which required one EM object with $E_T > 20 \text{ GeV}$ and $\cancel{E}_T > 20 \text{ GeV}$. Events were selected which had an isolated muon, one or more jets, and a tight or loose electron. All event selection cuts were applied with the exception of the trigger. The number of background events was then found by summing the E_T -dependent probability for a jet to have mimicked an electron for each event which passed the event selection criteria, accounting correctly for events which contained more than one jet and the difference in the integrated luminosities between the two triggers. The total number of background events expected from $e\mu + \text{jet}$ events was found to be $0.118 \pm 0.018(\text{stat}) \pm 0.035(\text{syst})$. Again, the systematic error is due to the uncertainty in the probability for a jet to mimic an electron.

TABLE III. Summary of the $WZ \rightarrow l\nu ll$ results. \mathcal{L} is the integrated luminosity, ϵ is the overall detection efficiency, Br is the branching ratio, N_{obs} is the number of events observed, N_{bkg} is the number of background events, and N_{SM} is the predicted number of SM events.

	$e\bar{e}e$	$\mu\nu ee$	Total
\mathcal{L}	92.3 ± 5.0 pb ⁻¹		
ϵ	0.169 ± 0.014	0.115 ± 0.014	
Br	0.36% ± 0.01%		
N_{obs}	1	0	1
N_{bkg}	0.38 ± 0.14	0.12 ± 0.04	0.50 ± 0.17
N_{SM}	0.15 ± 0.01	0.10 ± 0.01	0.25 ± 0.02

The total background to $WZ \rightarrow \text{trileptons}$ was 0.50 ± 0.17 events.

D. Efficiency estimate

The efficiency estimate was made using a leading-order Monte Carlo (MC) event generator [2] which also could simulate the effects of anomalous couplings. The Martin-Roberts-Stirling set D'_\perp (MRSD $'_\perp$) parton distribution functions [31] were used. To correct for the effects of higher-order QCD processes which contribute to WZ production, the resulting cross section was increased by a k factor of 1.34 [2] and the WZ system was given a transverse boost according to the distribution produced by the PYTHIA Monte Carlo [32] simulation of SM WZ production. A parametrized detector simulation was used to account for the acceptance of the detector, the effects of detector resolution on the measurements of charged leptons and \cancel{E}_T , and the length ($\sigma \sim 30 \text{ cm}$) of the $p\bar{p}$ collision region along the beam direction.

For SM WZ production, the detection efficiency in the $e\bar{e}e$ and $\mu\nu ee$ channels was found to be $(16.9 \pm 1.4)\%$ and $(11.5 \pm 1.4)\%$, respectively. For a SM cross section of 2.6 pb [33], the $(W \rightarrow l\nu) \times (Z \rightarrow ee)$ branching fractions [34], and an integrated luminosity of $92.3 \pm 5.0 \text{ pb}^{-1}$, the expected number of events in the $e\bar{e}e\nu$ and $e\bar{e}\mu\nu$ channels was $0.146 \pm 0.002(\text{stat}) \pm 0.012(\text{syst})$ and $0.099 \pm 0.001(\text{stat}) \pm 0.009(\text{syst})$, respectively. The small statistical uncertainties reflected the large number of MC events generated and processed through the detector simulation. The systematic error included the uncertainties in the luminosity (5.3%), the particle identification efficiency (0.7%), the trigger efficiency (2%), the branching fraction (3.7%), and the MC cross section due to the choice of the parton distribution function and Q^2 scale (5%). The total expected signal from SM WZ production was 0.25 ± 0.02 events. The results are summarized in Table III.

E. WZ production cross section limit

The 95% confidence level (C.L.) upper limit on the WZ cross section is estimated based on one observed event and a subtraction of the expected background of 0.50 ± 0.17 events. Poisson-distributed numbers of events were convoluted with

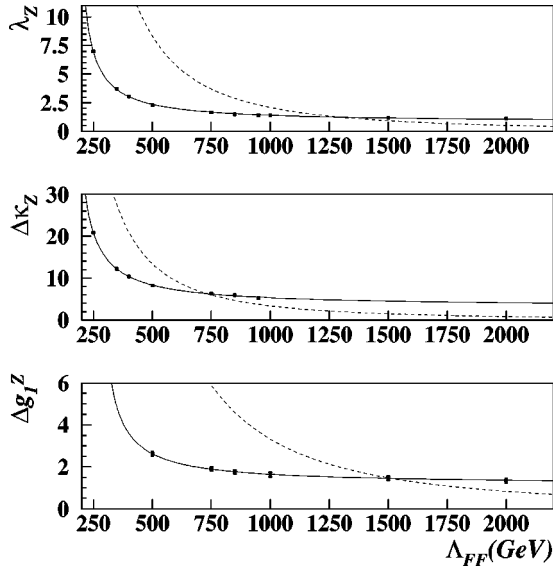


FIG. 3. One-dimensional 95% C.L. (solid) and unitarity limits (dashed) vs Λ for the WWZ coupling parameters λ_Z , $\Delta\kappa_Z$, and Δg_1^Z .

Gaussian uncertainties in the efficiency and background. For WZ production, the 95% C.L. upper limit on the cross section was 47 pb, consistent with, but much larger than, the SM prediction.

F. Limits on anomalous WWZ couplings

The event generator [2] and parametrized detector simulation were used, in a manner identical to that described above, to find the efficiency and expected number of events in the case of hypothetical anomalous WZ couplings. A grid in the $\lambda_Z - \Delta g_1^Z$ plane was used. Once the probability for observing one event was determined [30] for each point in the grid, limits on the anomalous couplings were made. The limits were found by taking the logarithm of the likelihood and identifying the contour in $\lambda_Z - \Delta g_1^Z$ around the point of maximum of the logarithm of the likelihood (L_{\max}) where $L = L_{\max} - \delta$. To set a 95% C.L. limit in one dimension, the contour was evaluated at $\delta = 1.92$. To set a 95% C.L. limit in two dimensions (allowing two anomalous couplings to vary at the same time), the contour was evaluated at $\delta = 3.00$.

The value of the form factor scale Λ was chosen such that the coupling limit was less than the unitarity limit [35]. The one-dimensional 95% C.L. coupling limits and unitarity limits as a function of Λ for each of the three coupling parameters are shown in Fig. 3.

This analysis was most sensitive to the parameters λ_Z and Δg_1^Z . Setting $\Lambda = 1$ TeV, the one-dimensional 95% C.L. limits from the $e\bar{e}e$ and $\mu\nu e\bar{e}$ channels are

$$|\Delta g_1^Z| < 1.63$$

$$|\lambda_Z| < 1.42$$

when all other parameters are held at their SM values. The two-dimensional 95% C.L. contour limits for $\Lambda = 1$ TeV are shown in Fig. 4 for the $e\bar{e}e$ and $\mu\nu e\bar{e}$ data combined.

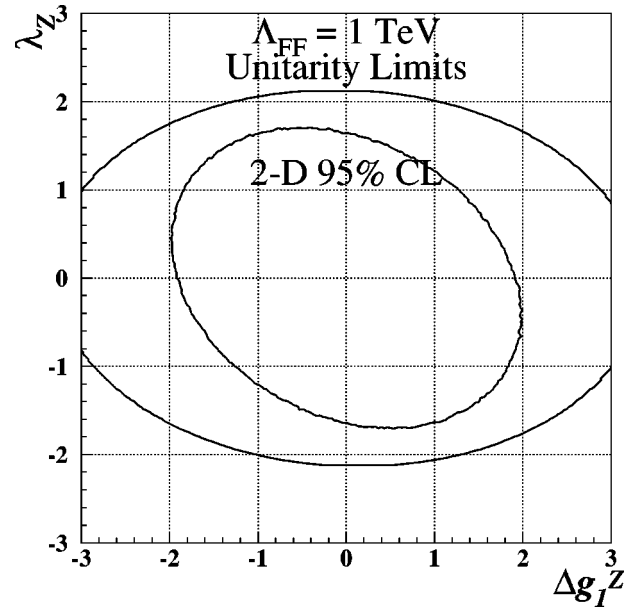


FIG. 4. Correlated limits on Δg_1^Z and λ_Z for $\Lambda = 1$ TeV obtained from a fit to the cross section using the 1994–1996 data for the $\mu\nu e\bar{e}$ and $e\bar{e}e$ channels combined. The inner solid line is the two-dimensional 95% C.L. limit and the outer solid line is the unitarity limit.

V. SEARCH FOR ANOMALOUS WW AND WZ PRODUCTION

The 1994–1995 data were searched for anomalous WW/WZ production in events with the signature: high- p_T muon; large E_T ; and at least two jets ($\mu\nu jj$).

A. Trigger and data sample

The level 1 trigger consisted of a muon candidate in the central region and at least 5 GeV deposited in a hadronic trigger tower ($\Delta\eta \times \Delta\phi = 0.2 \times 0.2$). As the muon scintillation counters became available during the collider run they were added to the level 1 trigger in such a way as to veto out-of-time muons, such as those that originated from cosmic rays.

The level 2 trigger required a muon with $p_T > 10$ GeV/ c , as determined by the muon pattern recognition algorithm taken from the reconstruction program. A jet was required with $E_T > 15$ GeV within the region $|\eta| < 2.5$. The jets were identified by a cone algorithm which summed E_T 's of calorimeter towers in cones of $R = 0.7$. The efficiency of the jet part of the level 1 and level 2 triggers was measured as a function of the reconstructed jet E_T in three separate pseudorapidity bins by comparing the results of the single-muon trigger with the single-muon plus jet trigger for events which contained a single jet. Figure 5 shows the jet trigger efficiency as a function of jet E_T for the pseudorapidity region $|\eta| < 1.0$. The jet trigger efficiency reached a plateau at jet E_T of approximately 40 GeV. The efficiency was parametrized using an error function. The curve shown in Fig. 5 is the result of that fit. The results in the other two pseudorapidity regions were similar. For SM Monte Carlo events

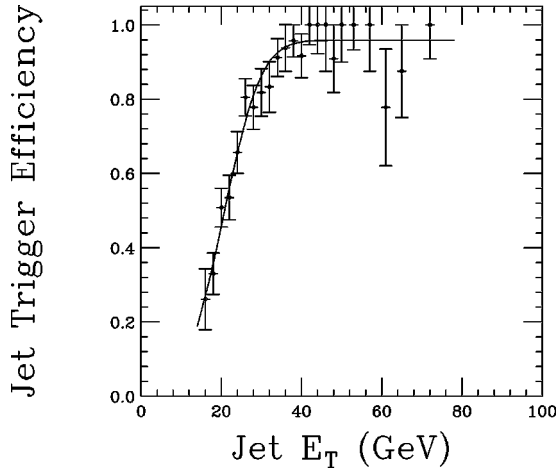


FIG. 5. Jet trigger efficiency in pseudorapidity region $|\eta| < 1.0$. The curve is the result of an error function fit to the efficiency.

which passed all of the selection criteria, the efficiency of the jet part of the trigger was 0.927 ± 0.007 . An alternate fit with a plateau at 100% increased this efficiency by 0.012 and that was taken as a systematic uncertainty. The efficiency of the muon component of the trigger, determined from a sample of muons collected using triggers which did not require any muons, was 0.707 ± 0.018 . The integrated luminosity [29] of the data sample was $80.7 \pm 4.3 \text{ pb}^{-1}$.

B. Event selection criteria

The signature of the muon+jets channel consisted of an isolated high- p_T muon from the W boson decay and a minimum of two jets from a W or Z boson decay. We did not differentiate between the two processes $W \rightarrow jj$ and $Z \rightarrow jj$ due to the dijet mass resolution of the calorimeter. Single muon events with the following characteristics were selected. The muon was within the central region, which corresponded approximately to $|\eta| < 1$, and had transverse momentum $p_T^\mu \geq 20 \text{ GeV}/c$. A E_T of at least 20 GeV was required in each event. Demanding a transverse mass $M_T(\mu\nu) > 40 \text{ GeV}/c^2$, where

$$M_T(\mu\nu) = \sqrt{2E_T^\mu E_T[1 - \cos(\phi_\mu - \phi_\nu)]},$$

completed the kinematic selection defining the decay of a W boson candidate. Next, the candidates had to contain at least two jets ($|\eta| < 2.5$) with $E_T \geq 20 \text{ GeV}$. The invariant mass of the two highest E_T jets had to be between 50 and 110 GeV/c^2 as expected for the decay of a W or Z boson. Figure 6 displays the distribution of the invariant mass of the two highest E_T jets in the 372 events which remained in the sample after all selection criteria, except for the dijet mass selection, had been applied.

Last, application of the dijet mass cut led to a final data sample of 224 events. The $p_T(\mu\nu)$ distribution for these events is shown in Fig. 7. The distribution indicates absence of events at $p_T(\mu\nu) > 150 \text{ GeV}/c$. The W boson candidate with the highest transverse energy had $p_T(\mu\nu) = 141 \text{ GeV}/c$.

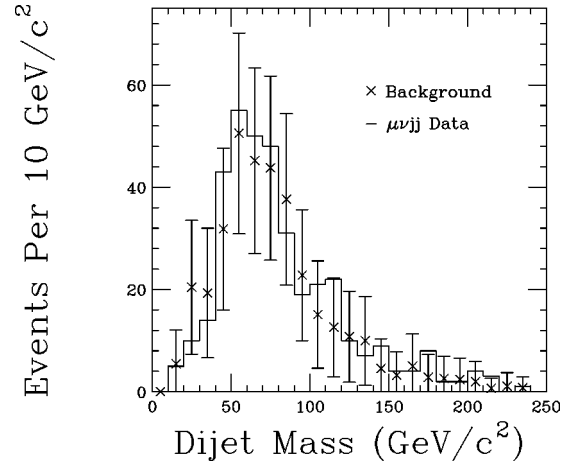


FIG. 6. Comparison of invariant mass of the two highest E_T jets for the data (histogram) and the estimated total background (points with uncertainties) for the $WW/WZ \rightarrow \mu\nu jj$ channel. The uncertainties shown are statistical only.

C. Background expected

There were two major sources of background to the $WW/WZ \rightarrow \mu\nu jj$ production: $W + \geq 2$ jets with $W \rightarrow \mu\nu$ and QCD multijet events where one of the jets was accompanied by a muon which was misidentified as an isolated muon and where there was significant E_T . The latter background could have arisen from b -quark pair production, for instance. Contributions from other backgrounds such as $t\bar{t}$ production with subsequent decay to $W^+ b W^- \bar{b}$ followed by $W \rightarrow \mu\nu$; WW/WZ production with $W \rightarrow \tau\nu$ followed by $\tau \rightarrow \mu\nu\bar{\nu}$; $ZX \rightarrow \mu\mu X$, where one of the muons was missing; and $ZX \rightarrow \tau\tau X$ with $\tau \rightarrow \mu\nu\bar{\nu}$, were small or negligible.

The QCD multijet background was estimated using a background enriched data sample. This technique was similar to that used in our previous analysis [36]. The probability for a jet with a muon to be misidentified as an isolated muon

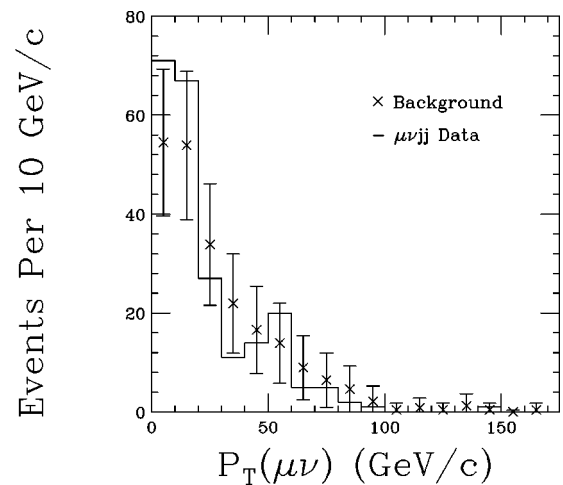


FIG. 7. Comparison of the $p_T(W)$ distributions of signal (histogram) and estimated total background (\times with statistical uncertainties) for $WW/WZ \rightarrow \mu\nu jj$. They are consistent with each other indicating the presence of no significant anomalous gauge couplings.

was determined from the ratio of the number of events containing an isolated muon, at least one jet, and \cancel{E}_T less than 20 GeV to the number of events which contained a muon which failed the jet isolation requirement (but otherwise passed the muon identification cuts), two or more jets, and \cancel{E}_T less than 20 GeV. This probability was 0.041 ± 0.007 . Then the number of events which passed all of the selection criteria of the signal except for the muon-jet isolation requirement, again applied in reverse so as to form a sample complementary to the signal, was counted. This provided the sample of events for which misidentification of a non-isolated muon as an isolated muon would have created a false signal. There were 2567 such events. Thus the QCD multijet background was 105 ± 19 (stat) events. The QCD multijet background was also calculated for events which passed all the selection criteria for the signal except for the dijet invariant mass selection, which was applied in reverse. This number was necessary for performing a background subtraction to the data in the out-of-mass cut region in order to calculate a normalization factor for the $W + \geq 2$ jets background. The QCD multijet background in the out-of-mass cut region was 55 ± 14 (stat) events.

The $W + \geq 2$ jets background was estimated using the VECBOS [37] event generator, with $Q^2 = (p_T^j)^2$, followed by parton fragmentation using the HERWIG [38] package and a detailed GEANT-based [39] simulation of the detector. Normalization of the $W + \geq 2$ jets background was determined by comparing the number of events expected from the VECBOS estimate to the number of candidate events outside the dijet mass window, after the QCD multijet contribution had been subtracted. The contribution from this background was calculated to be 117 ± 24 (stat) events. A small component of the background, due to $Z + \geq 2$ jets with an unreconstructed muon which mimicked the \cancel{E}_T , was accounted for in this procedure because of the kinematic similarity to W boson decay.

Among the other backgrounds, the only non-negligible contribution arose from $t\bar{t} \rightarrow W^+ b W^- \bar{b}$ decays. This was estimated using a Monte Carlo sample produced similarly to that of the $W + \geq 2$ jets background sample. The $t\bar{t}$ background, calculated assuming a cross section of 5.5 ± 1.8 pb [40], amounted to 2.7 ± 1.2 events.

The total expected background was 224 ± 31 (stat) events. The number of observed events (224) was consistent with the background, and was much larger than the predicted SM WW/WZ signal (discussed in the next section). The systematic uncertainties in the QCD multijet background and the $W + \geq 2$ jets background were correlated because of the common uncertainty in the jet energy scale and because of the background subtraction carried out in the normalization procedure when the $W + \geq 2$ jets background was determined. As a cross-check, the consistency between the background estimate and the number of observed events was verified for variations of the event selection criteria. The systematic uncertainties for the background estimation were dijet mass window selection (13.4%), muon isolation (11.7%), jet energy scale (7.8%), missing transverse energy selection (7.2%), and W boson transverse mass selection

TABLE IV. Comparison of signal (data) and backgrounds for the mode $WW/WZ \rightarrow \mu\nu jj$. The data sample is consistent with the SM prediction and estimated backgrounds showing no evidence for anomalous gauge couplings.

Sample	Number of events
QCD multi-jet background	105 ± 19 (stat)
$W + \geq 2$ jets background	117 ± 24 (stat)
$t\bar{t}$ background	2.7 ± 1.2 (stat)
Total background	224 ± 31 (stat) ± 46 (syst)
SM prediction	4.5 ± 0.8 (stat+syst)
Observed data sample (luminosity=80.7 pb ⁻¹)	224

(4.3%). The total systematic uncertainty in the background was 46 events and the total uncertainty in the background was 56 events.

The contributions from all background sources are shown in Table IV. The estimates in the table for the components of the background include statistical uncertainties only. Figure 6 also displays the invariant mass of the two highest- E_T jets from the expected background with all selection criteria, except for the dijet invariant mass selection, applied. The final distributions of the signal and the sum of backgrounds are plotted as a function of $p_T(W)$ in Fig. 7.

D. WW/WZ signal estimate

The efficiency for detecting WW and WZ events, for both SM and anomalous couplings, was determined using a leading-order event generator [2] and a parameterized simulation of the detector. The MRSD' parton distributions [31] and a k factor of 1.34 [2] were used in estimating the WW/WZ cross section. In order to simulate the kinematics associated with higher-order production processes, the diboson decay products were boosted in the direction opposite to the hadronic recoil according to the E_T distribution provided by PYTHIA [32] for SM WW production. The efficiency was 2.5% lower when this boost was turned off, and half of this difference was taken as the fractional systematic uncertainty. The interaction points were selected around the center of the nominal collision point ($z=0$) from a Gaussian distribution with $\sigma=30$ cm.

The muon fiducial acceptance was determined from a GEANT-based [39] detector model and is shown in Fig. 2.

The jets from a high- $p_T W$ or Z boson decay may have been close enough to overlap and have poorly reconstructed energies, or they may have been completely merged into one jet. Therefore, the efficiencies of the jet selection and dijet mass selection depended on the boson's p_T . SM WW events, generated using PYTHIA Monte Carlo program and the GEANT-based detector model, were used to determine this efficiency as a function of $p_T(\mu\nu)$. The results were incorporated into the parameterized detector simulation. Figure 8 shows the efficiency as a function of $p_T(\mu\nu)$ for events which passed the rest of the event selection criteria. The efficiency was low for low- $p_T W$ boson events because of the jet E_T threshold of 20 GeV. It peaked at 63% for

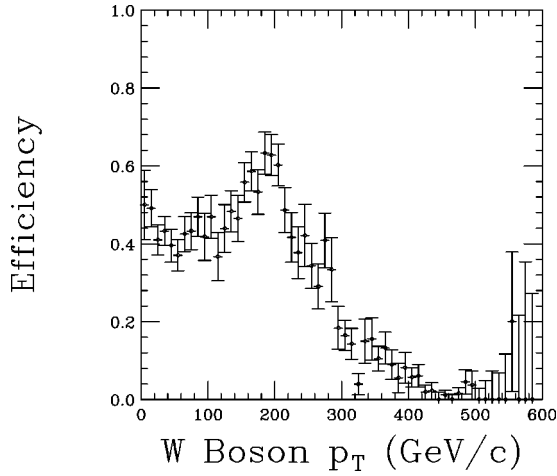


FIG. 8. The efficiency of the dijet reconstruction and selection as a function of $p_T(\mu\nu)$ in the $WW/WZ \rightarrow \mu\nu jj$ analysis. The uncertainties shown are statistical only.

$p_T(\mu\nu) = 200$ GeV/ c and fell for higher p_T because of jet merging. The uncertainty in the jet energy scale corrections led to a systematic uncertainty in the efficiency for W and Z boson identification of 3%.

The kinematic efficiencies for SM WW and WZ detection were $0.073 \pm 0.002(\text{stat}) \pm 0.003(\text{syst})$ and $0.067 \pm 0.002(\text{stat}) \pm 0.010(\text{syst})$, respectively, where the additional systematic uncertainty originates from differences between the acceptances calculated with the parametrized detector simulation and the acceptances calculated using PYTHIA and GEANT due to the jet reconstruction efficiency parametrization. Folding in the uncertainties due to the model of the jet trigger, the jet energy scale, and in the initial diboson boost, the systematic uncertainties in the kinematic efficiency amounted to 6.7% and 15.8% of the WW and WZ detection efficiency. Thus, the total efficiencies for SM WW and WZ production were $0.0351^{+0.0033}_{-0.0048}$ and $0.0322^{+0.0055}_{-0.0064}$, respectively. The efficiency was slightly higher for simulated WW and WZ production with anomalous $WW\gamma$ and/or WWZ couplings because the bosons originated at higher average p_T . For instance, for WW events produced with $\Lambda = 2.0$ TeV, the total efficiency was $0.038^{+0.004}_{-0.005}$ for the case $\lambda = 1.0$ and $\Delta\kappa = 0.0$, and $0.043^{+0.004}_{-0.006}$ for the case $\lambda = 2.0$ and $\Delta\kappa = 2.0$.

The predicted cross section [2] for SM WW (WZ) production is 10.1 (2.6) pb. A 5% systematic uncertainty in this originates from the variation of the cross section depending on the set of parton distributions used in the event generation. The branching fractions [34] for $W \rightarrow \mu\nu$ and $W \rightarrow \text{jets}$ or $Z \rightarrow \text{jets}$ lead to overall branching fractions of 0.1412 ± 0.0086 and 0.0727 ± 0.0042 , respectively. Therefore, with an integrated luminosity of $80.7 \pm 4.3 \text{ pb}^{-1}$, $4.04^{+0.54}_{-0.68}$ WW events and $0.49^{+0.10}_{-0.11}$ WZ events were expected to have been detected if production is solely through SM processes.

E. Limits on anomalous $WW\gamma$ and WWZ couplings

Since no excess of events in the high- $p_T(W)$ region was observed, significant deviations from the SM trilinear gauge

TABLE V. Axis limits (one-dimensional) at the 95% C.L. with two assumptions for the relation between the $WW\gamma$ and WWZ couplings ($WW\gamma = WWZ$ and HISZ) and for two different values of Λ in the mode $WW/WZ \rightarrow \mu\nu jj$.

Coupling	$\Lambda = 1.5$ TeV	$\Lambda = 2.0$ TeV
$\lambda_\gamma = \lambda_Z$	-0.45, 0.46	-0.43, 0.44
$\Delta\kappa_\gamma = \Delta\kappa_Z$	-0.62, 0.78	-0.60, 0.74
$\lambda_\gamma = \lambda_Z$ (HISZ)	-0.44, 0.46	-0.42, 0.44
$\Delta\kappa_\gamma$ (HISZ)	-0.75, 0.99	-0.71, 0.96

couplings were excluded. Using the detection efficiencies for SM WW and WZ production and the background subtracted data, upper limits were set on the anomalous coupling parameters λ and $\Delta\kappa$. This determination was made using a binned likelihood fit of the observed $p_T(W)$ spectrum to the prediction of the Monte Carlo signal plus the estimated background. Unequal width bins were used to evenly distribute the observed events, especially those in the high $p_T(W)$ region. In each p_T bin for a given set of anomalous coupling parameters, the probability for the sum of the background estimate and Monte Carlo WW/WZ prediction to fluctuate to the observed number of events was calculated. The uncertainties in the background estimations, efficiencies, integrated luminosity, and Monte Carlo signal modelling were convoluted into the likelihood function using Gaussian distributions.

The one-dimensional 95% C.L. limits on λ and $\Delta\kappa$ are summarized in Table V for $\Lambda = 1.5$ TeV and 2.0 TeV. The first two rows provide the coupling limits in the case of equal couplings for WWZ and $WW\gamma$. The last two rows provide limits in the case of HISZ relations [5]. In each case, one of the couplings was fixed to its SM value while the other was varied. The two-dimensional bounds (corresponding to a logarithm of the likelihood function value 3.00 below the maximum value) for anomalous coupling parameters in the λ - $\Delta\kappa$ plane are shown in Fig. 9 for $\Lambda = 1.5$ TeV. Figure 9 also shows the bounds imposed by the unitarity conditions as a larger ellipse.

VI. COMBINED RESULTS

The results of the two searches described in this paper have been combined with those of our previous publications

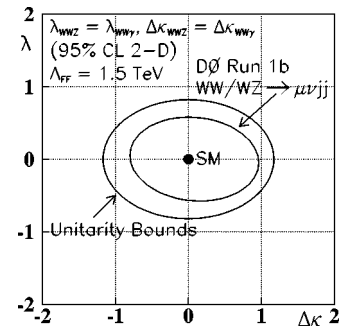


FIG. 9. Contour plot of allowed region in the $\lambda - \Delta\kappa$ space for $WW/WZ \rightarrow \mu\nu jj$ at 95% C.L. for $\Lambda = 1.5$ TeV. The outer ellipse shows the bounds imposed by the unitarity relations on λ and $\Delta\kappa$.

TABLE VI. One-dimensional limits at 95% C.L. from a simultaneous fit to the $D\bar{O}$ $W\gamma$, $WW \rightarrow$ dilepton, $WW/WZ \rightarrow e\nu jj$, $WW/WZ \rightarrow \mu\nu jj$, and $WZ \rightarrow$ trilepton data samples. The HISZ results included the additional constraint $\alpha_{B\phi} = \alpha_{W\phi}$.

Coupling	$\Lambda = 1.5$ TeV	$\Lambda = 2.0$ TeV
$\lambda_\gamma = \lambda_Z$ ($\Delta\kappa_\gamma = \Delta\kappa_Z = 0$)	-0.20, 0.20	-0.18, 0.19
$\Delta\kappa_\gamma = \Delta\kappa_Z$ ($\lambda_\gamma = \lambda_Z = 0$)	-0.27, 0.42	-0.25, 0.39
λ_γ (HISZ) ($\Delta\kappa_\gamma = 0$)	-0.20, 0.20	-0.18, 0.19
$\Delta\kappa_\gamma$ (HISZ) ($\lambda_\gamma = 0$)	-0.31, 0.56	-0.29, 0.53
λ_Z (SM $WW\gamma$) ($\Delta\kappa_Z = \Delta g_1^Z = 0$)	-0.26, 0.29	-0.24, 0.27
$\Delta\kappa_Z$ (SM $WW\gamma$) ($\lambda_Z = \Delta g_1^Z = 0$)	-0.37, 0.55	-0.34, 0.51
Δg_1^Z (SM $WW\gamma$) ($\lambda_Z = \Delta\kappa_Z = 0$)	-0.39, 0.62	-0.37, 0.57
λ_γ (SM WWZ) ($\Delta\kappa_\gamma = 0$)	-0.27, 0.25	-0.25, 0.24
$\Delta\kappa_\gamma$ (SM WWZ) ($\lambda_\gamma = 0$)	-0.57, 0.74	-0.54, 0.69

using the procedure described in Ref. [12]. The method was to perform a binned maximum likelihood fit of the number of events and their kinematic characteristics to the expected signals and backgrounds, taking care to account for correlated uncertainties among the data sets. The number of events and the expected background in the $WZ \rightarrow$ trileptons analysis of Sec. IV and the $p_T(\mu\nu)$ spectrum as well as the expected background in the WW/WZ analysis of Sec. V were included into the multiple final state fit described in Ref. [13]. The resulting limits on anomalous couplings represent the most restrictive available from our experiment.

Sets of limits were produced using the range of assumptions about the relations between the couplings as discussed in Sec. I. Table VI contains limits on λ , $\Delta\kappa$, and where applicable on Δg_1^Z , for $\Lambda = 1.5$ and 2.0 TeV under each of the following assumptions: that the $WW\gamma$ couplings were equal to the WWZ couplings, that the $WW\gamma$ couplings were related to the WWZ couplings through the HISZ equations (with the additional constraint $\alpha_{B\phi} = \alpha_{W\phi}$), that the $WW\gamma$ couplings were at the SM values (producing limits on the WWZ couplings), and that the WWZ couplings were at the SM values (producing limits on the $WW\gamma$ couplings). Figure 10 shows the two-dimensional limit contours and one-dimensional limit points for λ vs $\Delta\kappa$ for these four relationships between the $WW\gamma$ and WWZ couplings. Table VII contains limits on $\alpha_{B\phi}$, $\alpha_{W\phi}$, α_W , and Δg_1^Z for $\Lambda = 1.5$ and 2.0 TeV. Figure 11 shows the two-dimensional limit contours and one-dimensional limit points for α_W vs $\alpha_{B\phi}$ when $\alpha_{W\phi} = 0$ and for α_W vs $\alpha_{W\phi}$ when $\alpha_{B\phi} = 0$. Note that the Fig. 11(a) limits on α_W vs $\alpha_{B\phi}$ are equivalent to limits on λ_γ vs $\Delta\kappa_\gamma$ because Δg_1^Z is fixed to zero. Also, for purposes of comparison with LEP experiments, the central values and 68% C.L. limits on λ_γ and $\Delta\kappa_\gamma$ were calculated under the HISZ relations (without the extra constraint $\alpha_{B\phi} = \alpha_{W\phi}$) for $\Lambda = 2.0$ TeV. They were $\lambda_\gamma = 0.00_{-0.09}^{+0.10}$ and $\Delta\kappa_\gamma = -0.08_{-0.34}^{+0.34}$.

VII. CONCLUSIONS

Using $p\bar{p}$ collisions at center-of-mass energy $\sqrt{s} = 1.8$ TeV detected with the $D\bar{O}$ detector, two gauge boson

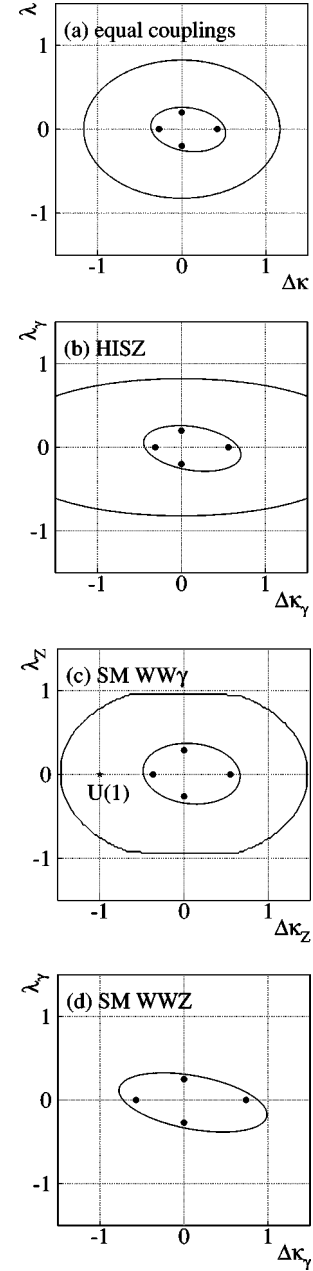


FIG. 10. Contour limits on anomalous couplings from a simultaneous fit to the $D\bar{O}$ $W\gamma$, $WW \rightarrow$ dilepton, $WW/WZ \rightarrow e\nu jj$, $WW/WZ \rightarrow \mu\nu jj$, and $WZ \rightarrow$ trilepton final states for $\Lambda = 1.5$ TeV: (a) $\Delta\kappa \equiv \Delta\kappa_\gamma = \Delta\kappa_Z$, $\lambda \equiv \lambda_\gamma = \lambda_Z$, (b) HISZ relations, (c) SM $WW\gamma$ couplings, and (d) SM WWZ couplings. (a), (c), and (d) assume that $\Delta g_1^Z = 0$. The solid circles correspond to 95% C.L. one degree of freedom exclusion limits. The inner and outer curves are the 95% C.L. two degree of freedom exclusion contour and the constraint from the unitarity condition, respectively. In (d), the unitarity contour is located outside of the boundary of the plot. The HISZ results include the additional constraint $\alpha_{B\phi} = \alpha_{W\phi}$.

pair production processes were studied and used to produce limits on anomalous trilinear gauge boson couplings.

A search for $WZ \rightarrow e\nu ee$ and $\mu\nu ee$ candidates yielded one candidate event where the expected signal from SM WZ production was 0.25 ± 0.02 events and the expected back-

TABLE VII. One-dimensional limits at 95% C.L. on α parameters from a simultaneous fit to the $D\bar{D}$ $W\gamma$, $WW\rightarrow$ dilepton, $WW/WZ\rightarrow e\nu jj$, $WW/WZ\rightarrow\mu\nu jj$, and $WZ\rightarrow$ trilepton data samples.

Coupling	$\Lambda=1.5$ TeV	$\Lambda=2.0$ TeV
$\alpha_{B\phi}$ ($\alpha_{W\phi}=\alpha_W=0$)	-0.73, 0.59	-0.67, 0.56
$\alpha_{W\phi}$ ($\alpha_{B\phi}=\alpha_W=0$)	-0.19, 0.38	-0.18, 0.36
α_W ($\alpha_{B\phi}=\alpha_{W\phi}=0$)	-0.20, 0.20	-0.18, 0.19
Δg_1^Z ($\alpha_{B\phi}=\alpha_W=0$)	-0.25, 0.49	-0.23, 0.47

ground was 0.50 ± 0.17 events. The 95% C.L. upper limit on the cross section was 47 pb, consistent with, but rather larger than the expected SM cross section. Based on the one observed event, the detection efficiency, and the expected background, limits on anomalous WWZ couplings were produced. The one-dimensional limits, at 95% C.L., are $|\Delta g_1^Z| \leq 1.63$ ($\lambda_Z=0$) and $|\lambda| \leq 1.42$ ($\Delta g_1^Z=0$) for $\Lambda=1.0$ TeV.

A search for anomalous $WW/WZ\rightarrow e\nu jj$ production was performed. The expected background of 224 ± 56 events was much larger than the expected SM WW and WZ signal of 4.5 ± 0.8 events. From the $p_T(\mu\nu)$ distribution of the 224 observed events, which had no significant deviation from the expected background plus SM signal, limits on anomalous $WW\gamma$ and WWZ couplings were produced. Under the assumption that the $WW\gamma$ couplings equal the WWZ couplings, the one-dimensional 95% C.L. limits were -0.43

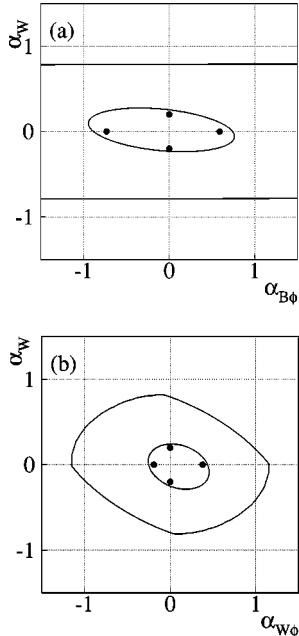


FIG. 11. Contour limits on anomalous couplings from a simultaneous fit to the $D\bar{D}$ $W\gamma$, $WW\rightarrow$ dilepton, $WW/WZ\rightarrow e\nu jj$, $WW/WZ\rightarrow\mu\nu jj$, and $WZ\rightarrow$ trilepton final states for $\Lambda=1.5$ TeV: (a) α_W vs $\alpha_{B\phi}$ when $\alpha_{W\phi}=0$ and (b) α_W vs $\alpha_{W\phi}$ when $\alpha_{B\phi}=0$. The solid circles correspond to 95% C.L. one degree of freedom exclusion limits. The inner and outer curves are the 95% C.L. two degree of freedom exclusion contour and the constraint from the unitarity condition, respectively.

TABLE VIII. Kinematic properties of the $WZ\rightarrow e\nu e e$ candidate event (run 89912, event 23020).

	e_1	e_2	e_3
E_T (GeV)	54.5	50.9	37.7
η	0.11	-0.62	1.37
ϕ	5.94	3.04	4.14

$\leq \lambda \leq 0.44$ ($\Delta\kappa=0$) and $-0.60 \leq \Delta\kappa \leq 0.74$ ($\lambda=0$) for $\Lambda=2.0$ TeV. Under the assumption that the $WW\gamma$ couplings are related to the WWZ couplings via the HISZ equations, the one-dimensional 95% C.L. limits were $-0.42 \leq \lambda \leq 0.44$ ($\Delta\kappa=0$) and $-0.71 \leq \Delta\kappa \leq 0.96$ ($\lambda=0$) for $\Lambda=2.0$ TeV.

The results of the two searches described in this paper have been combined with those from our previous publications to produce our most restrictive limits on anomalous $WW\gamma$ and WWZ couplings. Under the assumption that the $WW\gamma$ couplings equal the WWZ couplings, the one-dimensional 95% C.L. limits were $-0.18 \leq \lambda \leq 0.19$ ($\Delta\kappa=0$) and $-0.25 \leq \Delta\kappa \leq 0.39$ ($\lambda=0$) for $\Lambda=2.0$ TeV. Under the assumption that the $WW\gamma$ couplings are related to the WWZ couplings via the HISZ equations, the one-dimensional 95% C.L. limits were $-0.18 \leq \lambda \leq 0.19$ ($\Delta\kappa=0$) and $-0.29 \leq \Delta\kappa \leq 0.53$ ($\lambda=0$) for $\Lambda=2.0$ TeV. Limits on $\Delta\kappa$, λ , and Δg_1^Z were determined for the $WW\gamma$ couplings assuming the WWZ couplings are at the SM value and for the WWZ couplings assuming that the $WW\gamma$ couplings are at the SM value. Finally, limits on the $\alpha_{B\phi}$, $\alpha_{W\phi}$, and α_W anomalous couplings were produced.

ACKNOWLEDGMENTS

We thank the Fermilab and collaborating institution staffs for contributions to this work and acknowledge support from the Department of Energy and National Science Foundation (U.S.), Commissariat à l'Énergie Atomique (France), Ministry for Science and Technology and Ministry for Atomic Energy (Russia), CAPES and CNPq (Brazil), Departments of Atomic Energy and Science and Education (India), Colciencias (Colombia), CONACyT (Mexico), Ministry of Education and KOSEF (Korea), and CONICET and UBACyT (Argentina).

TABLE IX. Mass combination information for $e\nu e e$ candidate event. M_{e_i, e_j} is the invariant mass of electron i and electron j . M_{e_1, e_2, e_3} is the three-body mass of electron 1, electron 2, and electron 3. M_T is the transverse mass and p_T is the transverse momentum.

Mass combination information	
$M_{e_1, e_2} = 111.8$ GeV/c ²	$M_{e_1, e_2, e_3} = 171.7$ GeV/c ²
$M_{e_1, e_3} = 93.6$ GeV/c ²	$M_{e_2, e_3} = 112.4$ GeV/c ²
$\bar{E}_T = 46.2$ GeV	$\phi(\bar{E}_T) = 1.29$
$M_T(e_i, \bar{E}_T) = 73.0, 74.7, 82.6$ GeV/c ²	for e_1, e_2, e_3 respectively
$p_T(e_1, e_3) = 58.8$ GeV/c	$\phi(e_1, e_3) = -1.02$
$p_T(e_2, \bar{E}_T) = 63.0$ GeV/c	$\phi(e_2, \bar{E}_T) = 2.22$

APPENDIX: PARAMETERS OF THE WZ CANDIDATE EVENT

Given the expected signal to background ratio of approximately 1–2 in the channel $WZ \rightarrow e\bar{\nu}ee$, there is no certainty that the candidate event is actually due to WZ production. But because of the event's striking signature, it is described in detail in this appendix.

The candidate event contains three high- E_T electron can-

didates and large missing transverse energy (46.2 GeV). The event contains no other high- p_T objects (jets or muons). The properties of the candidate electrons are summarized in Table VIII. The missing transverse energy and the various mass combinations of the electrons with the missing transverse energy are listed in Table IX. The invariant mass of electron candidates 1 and 3 is $93.6 \text{ GeV}/c^2$, and the transverse mass formed using electron candidate 2 and the missing transverse energy is $74.7 \text{ GeV}/c^2$.

-
- [1] K. Hagiwara, R. D. Peccei, D. Zeppenfeld, and K. Hikasa, Nucl. Phys. **B282**, 253 (1987).
- [2] K. Hagiwara, J. Woodside, and D. Zeppenfeld, Phys. Rev. D **41**, 2113 (1990).
- [3] F. Boudjema *et al.*, Phys. Rev. D **43**, 2223 (1991).
- [4] Limits on anomalous couplings, presented in this paper, are given at the low energy limits of the couplings.
- [5] K. Hagiwara, S. Ishihara, R. Szalapski, and D. Zeppenfeld, Phys. Rev. D **48**, 2182 (1993). They parametrize WWZ couplings in terms of the $WW\gamma$ couplings: $\Delta\kappa_Z = \Delta\kappa_\gamma(1 - \tan^2 \theta_w)/2$, $\Delta g_1^Z = \Delta\kappa_\gamma/(2 \cos^2 \theta_w)$ and $\lambda_Z = \lambda_\gamma$.
- [6] DØ Collaboration, S. Abachi *et al.*, Phys. Rev. Lett. **75**, 1034 (1995).
- [7] DØ Collaboration, S. Abachi *et al.*, Phys. Rev. Lett. **78**, 3634 (1997).
- [8] DØ Collaboration, S. Abachi *et al.*, Phys. Rev. Lett. **75**, 1023 (1995).
- [9] DØ Collaboration, B. Abbott *et al.*, Phys. Rev. D **58**, 051101 (1998).
- [10] DØ Collaboration, S. Abachi *et al.*, Phys. Rev. Lett. **77**, 3303 (1996).
- [11] DØ Collaboration, B. Abbott *et al.*, Phys. Rev. Lett. **79**, 1441 (1997).
- [12] DØ Collaboration, S. Abachi *et al.*, Phys. Rev. D **56**, 6742 (1997).
- [13] DØ Collaboration, B. Abbott *et al.*, Phys. Rev. D **58**, 031102 (1998).
- [14] UA2 Collaboration, J. Alitti *et al.*, Phys. Lett. B **277**, 194 (1992).
- [15] CDF Collaboration, F. Abe *et al.*, Phys. Rev. Lett. **74**, 1936 (1995).
- [16] L3 Collaboration, M. Acciarri *et al.*, Phys. Lett. B **403**, 168 (1997).
- [17] CDF Collaboration, F. Abe *et al.*, Phys. Rev. Lett. **75**, 1017 (1995).
- [18] CDF Collaboration, F. Abe *et al.*, Phys. Rev. Lett. **78**, 4536 (1997).
- [19] L3 Collaboration, M. Acciarri *et al.*, Phys. Lett. B **398**, 223 (1997).
- [20] L3 Collaboration, M. Acciarri *et al.*, Phys. Lett. B **413**, 176 (1997).
- [21] OPAL Collaboration, K. Ackerstaff *et al.*, Phys. Lett. B **397**, 147 (1997).
- [22] OPAL Collaboration, K. Ackerstaff *et al.*, Eur. Phys. J. C **2**, 597 (1998).
- [23] OPAL Collaboration, K. Ackerstaff *et al.*, Eur. Phys. J. C **8**, 191 (1999).
- [24] DELPHI Collaboration, P. Abreu *et al.*, Phys. Lett. B **397**, 158 (1997).
- [25] DELPHI Collaboration, P. Abreu *et al.*, Phys. Lett. B **423**, 194 (1998).
- [26] ALEPH Collaboration, R. Barate *et al.*, Phys. Lett. B **422**, 369 (1998).
- [27] DØ Collaboration, S. Abachi *et al.*, Nucl. Instrum. Methods Phys. Res. A **338**, 185 (1994).
- [28] Pseudorapidity, η , is defined as $-\ln \tan \theta/2$ where θ is the polar angle. In the definition of the pseudorapidity of the calorimeter detector boundaries, the origin was the center of the calorimeter. In the definition of the pseudorapidity of an object such as an electron or muon, the origin was the $p\bar{p}$ collision point.
- [29] J. Bantly *et al.*, Fermilab Report No. TM-1995, 1997.
- [30] P. E. Gartung, Ph.D. thesis, University of California at Riverside, 1998 (unpublished), http://www-d0.fnal.gov/publications_talks/thesis/gartung/thesis.ps
- [31] A. D. Martin, R. G. Roberts, and W. J. Stirling, Phys. Rev. D **47**, 867 (1993).
- [32] T. Sjöstrand, "PYTHIA 5.6 and Jetset 7.3 Physics and Manual," Report No. CERN-TH.6488/92, 1992 (unpublished).
- [33] J. Ohnemus, Phys. Rev. D **44**, 3477 (1991).
- [34] Particle Data Group, R. M. Barnett *et al.*, Phys. Rev. D **54**, 1 (1996).
- [35] U. Baur (private communication). The unitarity limit contour was the ellipse where
- $$\Lambda = \left(\frac{4.33}{\lambda_Z^2 + \frac{M_W^2}{2M_Z^2} \Delta g_1^Z} \right)^{1/4}$$
- with Λ given in TeV.
- [36] DØ Collaboration, B. Abbott *et al.*, Phys. Rev. D **58**, 052001 (1998).
- [37] F. A. Berends *et al.*, Nucl. Phys. **B357**, 32 (1991).
- [38] G. Marchesini *et al.*, Comput. Phys. Commun. **67**, 465 (1992).
- [39] F. Carminati *et al.*, "GEANT User's Guide," CERN Program Library Long Writeup WS013 (1993) (unpublished).
- [40] DØ Collaboration, S. Abachi *et al.*, Phys. Rev. Lett. **79**, 1203 (1997).